

Astroclimate of specialized rooms at the Large Solar Vacuum Telescope. Part 2

V.V. Nosov,¹ V.M. Grigor'ev,² P.G. Kovadlo,² V.P. Lukin,¹
E.V. Nosov,¹ and A.V. Torgaev¹

¹*Institute of Atmospheric Optics,
Siberian Branch of the Russian Academy of Sciences, Tomsk*

²*Institute of Solar-Terrestrial Physics,
Siberian Branch of the Russian Academy of Sciences, Irkutsk*

Received November 28, 2007

Measurements of local astroclimate parameters in specialized rooms of the Large Solar Vacuum Telescope (Baikal Astrophysical Observatory ISTP SB RAS) are presented. It is shown that temperature gradients in the telescope rooms cause a Benard cell and the incipience of the turbulence in the pavilion of astronomical spectrograph. It is shown that the measurements confirm main stochastic scenarios (Landau–Hopf, Ruelle–Takens, Feigenbaum, and Pomeau–Menneville). The bifurcation Feigenbaum diagram is confirmed experimentally. The main vortex in the Benar cell is decomposed into smaller ones as a result of ten period-doubling bifurcations. The incipient turbulence is stated to be almost determinate. The fractal character of the turbulence spectrum is found. The actual atmospheric turbulence is shown to be a mixture of determined vortices of different scales, observed in the incipient turbulence. It has been found that the incipient turbulence introduces large errors into spectral measurements. The horizontal random shifts of spectral lines, appearing due to the pavilion effects, can reach 1 arc-second. The incipient turbulence approximates to the regular refraction by its optical properties due to low frequencies of line shifts.

Introduction

As is known,^{1–4} the atmosphere inside astronomic telescopes noticeably affects the quality of images.

This paper continues the work⁵ devoted to measurements and analysis of the of local astroclimate parameters of the most important working areas of specialized rooms of the Large Solar Vacuum Telescope (LSVT, Baikal Astrophysical Observatory ISTP SB RAS, Listvyanka village, Irkutsk Region). First of all, they are astronomic spectrograph (set up as the horizontal Ebert scheme and consisting of the indoor pavilion and the operator working place) and areas near the coordinate and adaptive tables.

In the first part of that work,⁵ the measurement schemes were described and measurement results were presented. It has been shown, that the Benard convection cell and the turbulence, incipient inside the astronomic spectrograph pavilion, are caused by temperature gradients inside the telescope rooms.

In the second part of the work, the properties of incipient turbulence are studied in detail; models of turbulent temperature spectrum are developed, the spectrum parameters (outer and inner scales, temperature fluctuation intensity) are studied. It is ascertain that measurement data confirm main stochastic scenarios (Landau–Hopf, Ruelle–Takens, Feigenbaum, and Pomeau–Menneville). In addition, the bifurcation Feigenbaum diagram is confirmed experimentally, and it is revealed that the main vortex in the Benar cell is decomposed into smaller

ones as a result of ten period-doubling bifurcations. The incipient turbulence is stated to be almost determinate. The fractal character (local self-similarity) of the turbulence spectrum is found experimentally. The actual atmospheric turbulence is shown to be a mixture of determined vortices of different scales, observed in the incipient turbulence.

The obtained results allow estimating the influence of atmosphere inside the telescope on the quality of astronomical observations. It is found that the incipient turbulence introduces large errors into spectral measurements, even on short paths. Horizontal random line shifts, appearing due to the pavilion effects, can reach 1 arc-second. In this case, lines shift slowly, with a frequency of about 0.01 Hz. Due to low shift of the frequencies, the incipient turbulence approximates to the regular refraction by its optical properties.

1. Models of temperature fluctuation spectra in the incipient turbulence

Models of temperature fluctuation spectra, first of all, of the spatial 3D spectrum $\Phi_T(\kappa)$, are required in problems of optical radiation propagation in undeveloped turbulence, including the forecasting of the influence of the telescope specialized rooms on the image quality.

As is known, time frequency spectra of temperature fluctuations $W_T(f)$ in open air are adequately described by the Karman model. The Kolmogorov developed turbulence spectra have a

long inertial interval, where $W_T \sim f^{-5/3}$ and the energy is transported from large-scale vortices to smaller ones.

Smoothed time frequency spectra of temperature fluctuations W_T are shown in Fig. 1 for a closed room and open air. As is seen, the closed-room spectra roll-off much more rapidly than open air ones within the inertial interval; besides, within the interval, there are only short individual frequency regions (in echelon), inside which the turbulence can be considered as Kolmogorov one ($W_T \sim f^{-5/3}$). These regions are observed between jumps of the spectral function at the frequencies, corresponding to local maxima of fluctuation correlation function (or minima of the structure function).

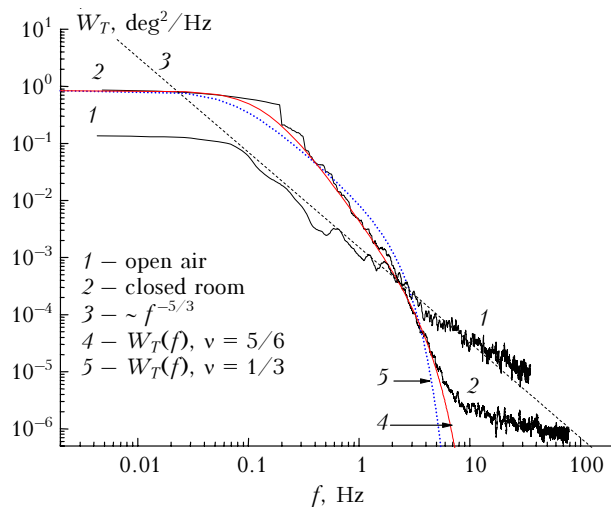


Fig. 1. Smoothed time frequency spectra of temperature fluctuations W_T in a closed room (point 5 in the pavilion) and in open air.

In case of smoothed echelons, experimental spectra of undeveloped turbulence have a number of characteristic regions of rapid power decreasing. Thus, if $W_T \sim \text{const}$ at a long energy interval, then first $W_T \sim f^{-8/3}$ with frequency rise (within the inertial interval) and then $W_T \sim f^{-12/3}$. Hence, energy transport from large to small vortices is insignificant in the incipient turbulence, i.e., the vortices are weakly diffused. Spectra roll-off slows down ($W_T \sim f^{-2/3}$) with further frequency rise, in the viscous interval, where the spectral density is close to the noise level. Similar behavior of spectra is observed at other points of the pavilion.

To construct a crude abstract model $\Phi_T(\kappa)$ of incipient turbulence spectra, the Karman model with roll-off corresponding to Fig. 1 within the inertial interval can be used. As is known,¹ the Karman one-dimensional spatial spectrum $V(\kappa)$ generally has a form

$$\begin{aligned}
 V(\kappa) &= V(0)(1 + \kappa^2/\kappa_0^2)^{-(\nu+1/2)} \exp(-\kappa^2/\kappa_m^2); \\
 \kappa_0 &= 2\pi/L_0, \quad \kappa_m = 5.92/l_0; \\
 V(0) &= B(0)\kappa_0^{-1} \Gamma(\nu + 1/2) \Gamma^{-1}(\nu) \pi^{-1/2},
 \end{aligned}
 \tag{1}$$

where L_0 and l_0 are the outer and inner turbulence scales, respectively; $V(0)$ is the spectrum value at zero; $B(0)$ is the dispersion of a random process; the parameter ν defines the roll-off rate in the inertial interval: $\nu = 1/3$ for the developed turbulence, then $V(\kappa) \sim \kappa^{-5/3}$ in the inertial interval. According to Fig. 1, $\nu = 5/6$ in the incipient turbulence, hence, $V(\kappa) \sim \kappa^{-8/3}$ in the most part of inertial interval. Further a more rapid spectrum roll-off ($V(\kappa) \sim \kappa^{-12/3}$) is described by the exponential factor in Eq. (1).

The maximum error of spectrum approximation by Eq. (1) falls into the region of very large frequencies (viscous interval). Therefore, problems of wave propagation, where this interval is of great importance, require a more detailed model as compared to Eq. (1). The viscous interval does not significantly contribute into problems of optical beam shift, image jitter, etc., i.e., where wave phase fluctuations play a key part; therefore, equation (1) can be used here.

Prescribe $\nu = 5/6$ in Eq. (1) and use the equation $W(f) = (4\pi/\nu)V(2\pi f/\nu)$ [Ref. 1] (where ν is the modulus of wind velocity), connecting the spatial spectrum $V(\kappa)$ with the time spectrum over positive frequencies $W(f)$. Then, the outer scale of the turbulence L_0 is retrieved from Eq. (1) (similarly to Ref. 3) at all measurement points in the pavilion from the experimental data on $W(0)$ and $B(0)$. However, the obtained values of L_0 do not give a good agreement between Eq. (1) and the experiment. The agreement can be attained when using frequency axis stretching in Eq. (1) $\kappa \rightarrow \xi\kappa$ with certain fitted stretch factor ξ ; then $L_0 \rightarrow \xi L_0$. Arising C_T^2 variations in this case are insignificant and fall within the measurement error limits.

The stretch factors ξ and resulted inner and outer turbulence scales are given in Table 1 for spectra (1) at $\nu = 5/6$ and $1/3$.

Table 1. Parameters of incipient turbulence spectra

Observation point	$\nu = 5/6$			$\nu = 1/3$		
	ξ	$L_0, \text{ cm}$	$l_0, \text{ cm}$	ξ	$L_0, \text{ cm}$	$l_0, \text{ cm}$
1	1.2	33.2	1.2	3.0	83.0	1.8
2	1.4	47.4	2.3	3.0	101.6	3.5
3	1.1	19.8	1.2	3.0	53.9	1.2
4	1.2	27.0	1.8	3.0	67.5	2.8
5	1.4	62.6	2.3	2.8	125.1	4.1
6	1.2	18.5	1.6	3.0	46.4	2.1
7	1.1	46.4	2.3	3.0	126.5	2.9
8	1.5	18.0	1.84	3.0	36.0	2.8
9	1.3	60.3	2.3	3.0	139.2	3.9
10	1.4	18.1	1.8	3.0	38.9	1.8
11	1.2	30.4	2.3	3.0	76.1	2.9
12	1.4	25.4	2.3	3.0	54.3	3.2

As is seen from Table 1, the inner scale of the incipient turbulence l_0 (mean $l_0 = 1.9 \text{ cm}$ at $\nu = 5/6$ and 2.7 cm at $\nu = 1/3$) is an order of magnitude larger than the outer one in free air ($0.7\text{--}4 \text{ mm}$, Refs. 1–3).

Model (1), which can be considered as a fluctuation spectrum in the incipient turbulence, better agrees with the experiment at $\nu = 5/6$ than at $\nu = 1/3$ (the developed turbulence). This follows from the comparison of curves 4 and 5 in Fig. 1. The area under the curves differs from the experimental one by 15% ($\nu = 5/6$) and 28% ($\nu = 1/3$). However, model (1) with $\nu = 1/3$ is commonly used and preferable, because it allows the extension of the wave propagation problem solution for the developed turbulence to the case of the incipient turbulence.

Using the equation

$$\Phi_T(\kappa) = -[1/(2\pi\kappa)]dV_T(\kappa)/d\kappa$$

and omitting exponentially small corrections, obtain the model of 3D temperature spectrum in the incipient turbulence:

$$\Phi_T(\kappa) = A_0 C_T^2 (\kappa^2 + \kappa_0^2)^{-(\nu+3/2)} \exp(-\kappa^2/\kappa_m^2),$$

$$A_0 = 0.033, \kappa_0 = 2\pi/L_0, \kappa_m = 5.92/l_0.$$

The L_0 and l_0 parameters of this spectrum for $\nu = 5/6$ and $\nu = 1/3$ are given in Table 1. It is evident, that $\Phi_T(\kappa) \sim \kappa^{-14/3}$ at $\nu = 5/6$ and $\Phi_T(\kappa) \sim \kappa^{-11/3}$ at $\nu = 1/3$ within the inertial interval. As for $V(\kappa)$, the spectrum $\Phi_T(\kappa)$ is more precise at $\nu = 5/6$.

The size distribution of outer turbulence scale L_0 in vertical plane inside the pavilion is shown in Fig. 2. Periodic behavior of the inner scale l_0 is similar to those shown in Fig. 2 for the outer one (see Table 1). In this case, the lower outer scale corresponds to the lower inner one.

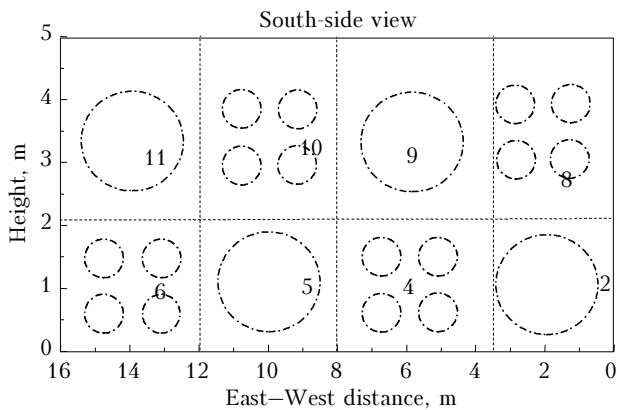


Fig. 2. Distribution of outer turbulence scale L_0 in the vertical plane passing through the pavilion center and west-east line (according to data from Table 1). Circles of larger diameter corresponds to larger L_0 values. Figures designate the numbers and positions of observation points.

It is known, that outer and inner scales determine maximum and minimum sizes of inhomogeneities. Hence, a spatial periodicity of sizes of temperature field inhomogeneities (of quincunx structure type) inside the pavilion follows from Fig. 2 and Table 1.

Regions with decreased outer scales can be called turbulence locks (or focuses), where an enhanced break-up of the large-scale averaged flow to smaller spatial components is observed. The intensity of random temperature variations, characterized by the periodic parameter C_T^2 (Ref. 5, Table 4, points 2, 4, 5, and 6), on average, decreases in the focuses, which is caused by smaller temperature differences (of passive admixtures^{1,2}) in more diffused and smaller vortices there.

2. Stochastic scenarios of convective flows

Compare the measurements in the pavilion with the well-known data on turbulence incipience from laminar flows (stochastic scenarios, most known of which are Landau–Hopf, Ruelle–Takens, Feigenbaum, and Pomeau–Menneville).² It will be shown below, that all these scenarios are confirmed in the incipient turbulence.

The Pomeau–Menneville scenario

As is known,^{2,6} as the distance increases (Reynolds number) in laminar flows in pipes, small turbulent regions with non-laminar flow first arise. These regions are usually called turbulent locks (or focuses). The locks become longer with increasing the distance and finally merge in a continuous turbulent flow. Turbulent locks are observed in experiments with other schemes as well.⁶ The locks cause alternation of laminar and turbulent modes. Such turbulence incipience via alternation is called the Pomeau–Menneville scenario.^{2,7}

It follows from our measurements, that turbulent locks and alternation (and, as follows from Ref. 5, Fig. 8, the corresponding bifurcations of stability change) exist in periodic flows in the Bernar cell as well. The parts of locks are played by regions with decreased spatial components (outer L_0 and inner l_0 scales). The locks turn out to be trapped in the structure of the Bernar cell and alternate with regions of large scales L_0 and l_0 . Hence, our data confirm the Pomeau–Menneville scenario.

The Landau–Hopf scenario

The incipient turbulence in the Bernar cell is a convenient model allowing one to trace the degradation of energy-carrying vortices into smaller ones. In fact, the toroidal vortex of averaged movements can be considered as the only energy-carrying vortex in the Bernar cell. Its sizes are determined by sizes of the room, where it originates. It is difficult to register the sizes of the main energy-carrying vortex in open air, because they depend on climate-forming factors. The outer turbulence scale is usually considered as this vortex, which itself is the product of the break-up.

The correlation factor b_T and the sample non-smoothed temperature frequency spectrum W_T , calculated from the pavilion measurements data (at point 5), are shown in Fig. 3.

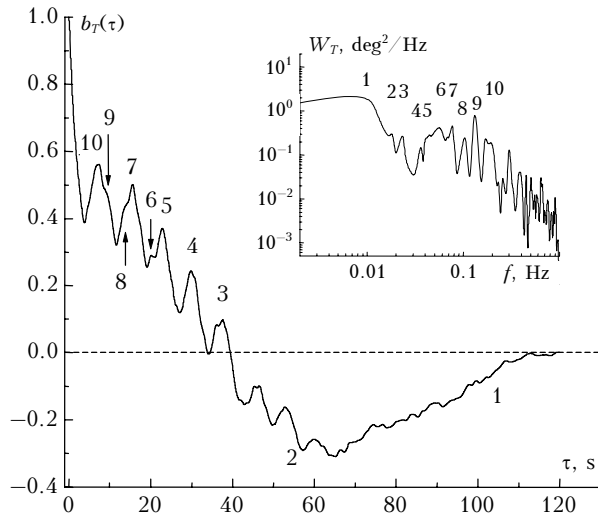


Fig. 3. Correlation factor b_T and non-smoothed frequency spectrum W_T (top right) in the pavilion (τ is the time). Figures designate the numbers of b_T and W_T maxima, corresponding to each other.

The correlation factor b_T has been calculated from different sample estimates,^{8–10} which, however, give no agreement between the results and reveal the local maxima of b_T . The correlation function can be calculated with an arbitrary small error at a large sample length N (a variance of b_T error is proportional to $1/N$). In our case, $N=19139$; hence, the 95% confidence bound of definition of the b_T function, shown in Fig. 3, makes ± 0.014 ; this is much less than b_T maxima.

The sample spectrum W_T was calculated without smoothing with a rectangular spectral window. As is known,^{8,9} such a window acts like a slit of about $2/T$ in width ($T = 120$ s). This resolution is sufficient to reveal the W_T spectrum maxima, uniquely corresponding to b_T maxima. Arguments of b_T and W_T maxima are related as $\tau_k f_k = 1$, $k = 1, 2, \dots$ (τ_1 and f_1 usually determine characteristic scales of b_T and W_T decrease). The diameter of the main energy-carrying vortex $2R_1$ is easily retrievable from the relation $2\pi R_1 = v\tau_1 = v/f_1$; it is equal to 294.4 cm ($v=9$ cm/s, $f_1=0.00973$ Hz) at point 5 in pavilion. Virtually the same result is obtained from data of Ref. 5, Fig. 7, if the trajectories of averaged movements are considered as circles.

Comparison of W_T spectra in Figs. 1 and 3, shows disappearance of real spectrum maxima at a standard spectrum smoothing by a wide window (dispersion of the smoothed spectrum in Fig. 1 is equal to 1% of the sample spectrum dispersion). Therefore, to calculate frequencies of spectrum maxima (harmonics), data of Fig. 3 are required. However, the rectangular spectrum window has large

side lobes, causing oscillations especially at high frequencies. It is possible to get rid of these lobes using any of extended nonrectangular windows (difference between them is negligible), for example, the Welch window.¹⁰ This window about two-fold decreases the dispersion as compared to a rectangular one and similarly widens the frequency band width. The widening is acceptable, because the band width turns out to be less than the mean width of spectrum maxima. This is evident from data for W_T in Fig. 3.

To improve the sample estimate, a digital threshold filter can be used additionally to eliminate weak (lower than the averaged in Fig. 1) harmonics in spectrum. These harmonics can be interpreted either as high frequency side lobes, incompletely damped by the Welch window, or a weakly pronounced transient process of energy-carrying vortex decomposition to smaller ones. It is shown below (see Fig. 6), that the structure of weak harmonics is fractal, it does not coincide with those of side lobes. Therefore, the side lobes are completely damped.

Analysis of the spectrum in Fig. 3 with the use of different spectrum windows shows that the spectrum maxima at frequencies lower than 0.17 Hz hold for almost all windows; therefore, the use of the threshold filter is justified at higher frequencies. Thus, the threshold filter extracts the main spectrum maxima (or first-order harmonics).

Based on the above analysis, harmonic frequencies (arguments of maxima) in the fluctuation spectrum W_T can be interpreted as frequencies of stable vortices observed in the temperature field (Fig. 4).

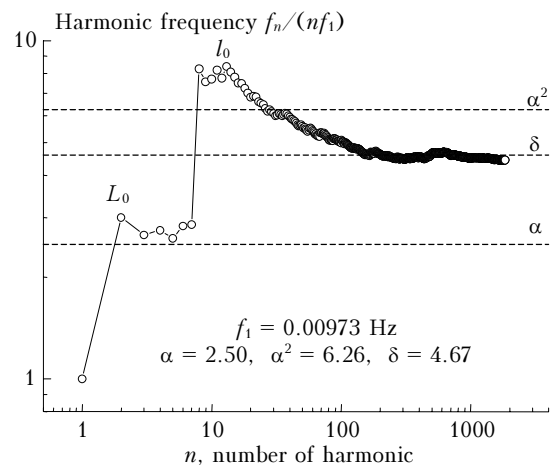


Fig. 4. Frequencies of the first-order stable vortices (harmonics) f_n in the fluctuation spectrum W_T .

The vortex frequencies f_n turn out to be multiple to the frequency of main energy-carrying vortex $f_1=0.00973$ Hz. Normalized to f_1 , they are natural numbers ($n = 1, 2, \dots$):

- $f_n/f_1 = 1, 6, 8, 11, 13, 17, 20, 31, 66, 68, 90, 93,$
- $109, 113, 117, 120, 127, 130, 133, 136, 144, 150,$
- $152, 157, 162, \dots$

(difference from integers does not exceed 0.03%, in the form of small corrections in the fourth, third, and second positions after point). An exact result of discrete break-up of the main energy-carrying vortex to smaller ones is multiple frequencies, from which the vortex diameters for each harmonics can be calculated by the equation $2\pi R_n = v/f_n$, $n = 1, 2, \dots$. They are shown in Fig. 5.

As shows the comparison of data in Fig. 5 and Table 1 (point 5, $v = 5/6$), the second frequency $6f_1$ approximately corresponds to the outer turbulence scale L_0 ($2R_1 = 294$ cm, $2R_2 = 49$ cm), while the frequencies $127f_1$ and $130f_1$ (terminating the inertial interval) – to the inner one l_0 ($2R_{17} = 2.3$ cm).

Vortices, which are degradation products of larger vortices (their frequencies are multiple to lower ones) are observed in the viscous interval and in a part of inertial one. For example,

$$f_n/f_2 = 11, 15, 20, 24, 25, \dots (n = 8, 11, 16, 21, 22, \dots);$$

$$f_n/f_3 = 15, 17, 18, 19, 36, \dots (n = 16, 20, 21, 23, 52, \dots).$$

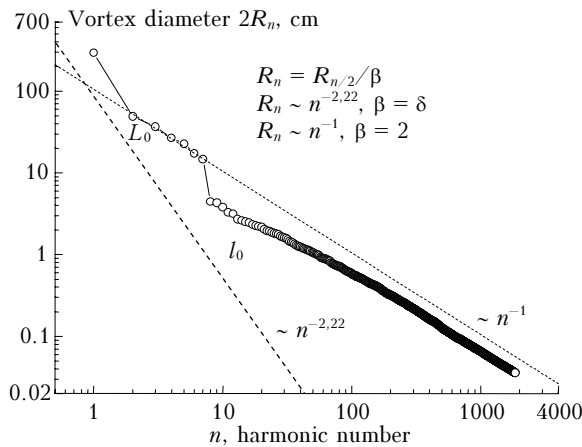


Fig. 5. Diameters of first-order stable vortices $2R_n$ in the fluctuation spectrum W_T .

The processes, observed inside the pavilion, are stable. Therefore, both the origination of vortex in the Bernar cell (due to a temperature gradient) and its break-up to smaller ones happen permanently (probably, with simultaneous self-replication). This evidently results in a threshold N -periodic flow with the frequencies f_n , $n = 1, 2, \dots, N$. Transformation of a small perturbation into a stable periodic flow follows from solutions of the Landau equation; the origination of time-periodic flows is called normal Hopf bifurcation. The Landau–Hopf scenario describes the incipience of turbulence as a sequence of normal bifurcations, generating a limiting N -periodic flow ($N \gg 1$) with, generally speaking, incommensurable frequencies.

However, the frequency (phase) incommensurability is usually unrealizable. Therefore, it is considered now that normal bifurcations generate consequent subharmonics.^{2,11} It is easily seen that our results confirm the Landau–Hopf scenario.

The Ruelle–Takens scenario

The Ruelle–Takens scenario can be considered as a refinement of the Landau–Hopf scenario. The difference is in the number of normal bifurcations, after which a flow can be considered as turbulent. According to the scenario, the turbulence occurs (a strange attractor appears) already after three normal bifurcations,^{2,12} i.e., a three-periodic flow ($N = 3$) can be already considered as turbulent. Then the convective flow becomes turbulent after origination of the main vortex in the Bernar cell and two events of its breakup.

The Feigenbaum scenario

The Feigenbaum scenario describes the turbulence incipience (appearance of a strange attractor) as a result of infinite consequence of period-doubling bifurcations.¹¹ These bifurcations appear only after magnitude change of a certain controlling parameter μ , e.g., Reynolds or Rayleigh numbers, etc. As is known, the Feigenbaum scenario follows from the universality of location of periodic points $x_0, (x_1^0, x_1^1), (x_2^0, x_2^1, x_2^2, x_2^3), \dots$ of 2^m -multiple cycles. These points x_m^k on the $x(\mu)$ curve correspond to tree branches, which symmetrically bifurcate at critical bifurcation points μ_m . Asymptotic similarity relations

$$\frac{x_m^k - x_m^{k+2^{m-1}}}{x_{m+1}^k - x_{m+1}^{k+2^m}} = \begin{cases} -\alpha, & 0 \leq k < 2^{m-1}, \\ \alpha^2, & 2^{m-1} \leq k < 2^m, \end{cases}$$

$$\sigma_m(\mu) = \frac{\mu_{m-1} - \mu_m}{\mu_m - \mu_{m+1}} = \delta, \quad \alpha = 2.503, \delta = 4.669$$

($m \gg 1$, α and δ are the Feigenbaum constants) are correct for both x and μ_m . Here x is usually (due to the universality) considered as the main parameter, characterizing a nonlinear dynamic structure, e.g., coordinates (in meters), or standard (m/s) or normalized speed ($\text{Hz} = 1/\text{s}$), as in the case of Navier–Stokes equations.

Though the equality $\sigma_m(\mu) = \delta$ is asymptotic, its suitability already after two–three period doublings (up to several percents) has been shown.¹¹ The theory has a high predictability due to the large rate of convergence δ ($\delta = 4.67$). For approximate evaluation, this equality can be used at $m \geq 0$. It is obvious that the equation $\sigma_m(\mu) = \delta$ has the solution $\mu_m = c\delta^{-m} + \mu_\infty$, $c = \text{const}$. Taking $m = 0, 1$ in the solution, we obtain a set of equations to find the constants c and μ_∞ . Hence, $c = \mu_0 - \mu_\infty$ and $\mu_\infty = \mu_0 + (\mu_1 - \mu_0)\delta/(\delta - 1)$. As is known, one can take $\mu_0 = 1$ and $\mu_1 = 3$ for the logistic equation $x_{m+1} = \mu x_m(1 - x_m)$, considered in Ref. 11, hence, $\mu_\infty = 3.54508$, which insignificantly differs from the exact value $\mu_\infty = 3.56994$, obtained in Ref. 11. Note, that μ_m (at $\mu_\infty \geq 0$) can both increase ($c < 0$) and decrease ($c > 0$) with increase of m .

In our case, the value of the controlling parameter μ is fixed (pavilion sizes, temperature gradient, etc. are preset) and, hence, we can observe only products of vortex break-up. Due to self-replicating of harmonics in the presence of doubling bifurcations, the harmonics, resulting from these bifurcations, are recordable.

Let, for example, the basic system parameter x be a shift with the length dimension. Then x_0 ($m = 0$) can be identified with the radius of the basic vortex R_1 . The following variables (x_1^0, x_1^1) are to be the products of x_0 break-up (nonsymmetrical bifurcation at $m = 1$). The only next largest radiuses R_2 and R_3 can play their parts (others are too small).

Hence, as it follows from the break-up diagram,¹¹ the pairs R_4, R_5 or R_5, R_6 (the first element in each pair is approximately equal to a half of R_2 and the second – to a half of R_3) can be chosen as the pair x_2^0, x_2^1 ($m = 2$).

Substituting these variables in the Feigenbaum equation, we obtain $(R_2 - R_3)/(R_4 - R_5) = 2.97$; $(R_2 - R_3)/(R_5 - R_6) = 2.30$. Another pair x_2^1, x_2^3 ($m = 2$) should be chosen from evident break-up products of the vortices with radiuses R_2 and R_3 (their frequencies are multiple to f_2 and f_3); R_8 and R_{16} correspond to the first break-up elements (see above). From the Feigenbaum equation, found $(R_2 - R_3)/(R_8 - R_{16}) = 6.11$.

Thus, though we are at the top of bifurcation tree ($m = 1, 2$), the obtained values of the modulus of left part of Feigenbaum equation are close to α and α^2 .

Note, that R_n satisfy the equation $R_n = R_{n/2}/\beta$ (see Fig. 5); In the inertial and viscous intervals $\beta \approx 2$. However, $\beta \approx \delta$ in the energy interval and in the inertial one near l_0 , hence, the equation $R_n = R_{n/2}/\delta$ agrees with the Feigenbaum similarity equation for the Fourier harmonics of x [Refs. 2 and 11].

The Feigenbaum constants α , α^2 , and δ are best pronounced in the harmonic frequency plot. As it is seen from Fig. 4, the normalized frequency $y_n = f_n/(nf_1)$ undergoes two large jumps with the rise in n . The first jump is observed near the outer turbulence scale L_0 (as a result, the frequency y_n is saturated to the level α) and the second one – near the inner scale l_0 (y_n is saturated to the level δ bypassing the level α^2). These jumps correspond to large steps of the function f_n/f_1 which can be interpreted as an analog of the “devilish staircase” (see Fig. 6). The presence of α , α^2 , and δ in Fig. 4 and the satisfaction the similarity equation confirm the Feigenbaum scenario.

Since $y_m \rightarrow \delta$ and $\sigma_m(\mu) \rightarrow \delta$ at $m \gg 1$, then bifurcation values of the controlling parameter μ_m can be connected with the harmonic frequencies f_m and vortex radiuses R_m , which are different parameters of the same turbulence incipience process. Actually, $|y_m - \delta| < \varepsilon$ and $|\sigma_{m^*} - \delta| < \varepsilon$ are should be true for some positive ε , δ_1 , and δ_2 as soon as $m^* > \delta_1$ and

$m > \delta_2$. Then $|y_m - \sigma_{m^*}| = |(y_m - \delta) - (\sigma_{m^*} - \delta)| \leq |y_m - \delta| + |\sigma_{m^*} - \delta| \leq 2\varepsilon$. Consequently, $\sigma_{m^*} \rightarrow y_m$. The levels δ_1 and δ_2 can be connected with each other, considering the domains of the confident convergence at sufficiently large m^* and m .

It is known^{2,11} that σ_{m^*} converges rapidly after several iterations, therefore, $m^* \approx 4-5$ can be taken as the domain of confident convergence. This determines the level δ_1 . As is evident from Fig. 4, the frequency y_m rapidly converges to δ near the inner scale l_0 at $m \approx 17 \div 30$ (level δ_2). Hence, levels δ_1 and δ_2 and numbers m^* and m are approximately related as $\delta_2 \approx 2^{\delta_1}$ and $m \approx 2^{m^*}$.

Taking these relations into account and solving the equation $\sigma_m(\mu) = y_n$, where $n \approx 2^m$, obtain

$$\mu_m = cy_n^{-m} + \mu_x, \quad y_n = f_n/(nf_1) = v/(2\pi n f_1 R_n), \quad (2)$$

$$c = \text{const}, \quad n \approx 2^m.$$

The constant c is determined here after the choice of μ , for example, in the form of the Reynolds number Re , Rayleigh number Ra , or others. For approximate estimates, equation (2) and $\sigma_m(\mu) = \delta$ are applicable at $m \geq 0$.

As an example, we show how equation (2) can be used provided μ is the Rayleigh number. Let $\mu_m = Ra_m/\text{const}$ in Eq. (2). The new constant simply leads to the overdetermination of c .

Let us observe the break-up process of the main vortex in the Benar cell to the level, when the existence of steady periodic flows (vortices) becomes impossible. In this case, the Ra number decreases from some maximum Ra_0 to the critical Ra_{cr} . In the process of breaking up, $Ra_m \ll Ra_{cr}$ at a sufficiently large m and, hence, Ra_x can be taken equal to zero in the first approximation. Then it follows from Eq. (2):

$$Ra_m = Ra_{m_0} y_{n_0}^{m_0} y_n^{-m},$$

where m_0 is the m value, at which Ra_{m_0} is known (since $n = 2^m$, then $n_0 = 2^{m_0}$). If $m_0 = 0$, then, according to the Feigenbaum numeration, Ra_{m_0} is the Rayleigh number for the main vortex in the Benar cell. This number can be roughly found, taking the layer thickness h in Ra definition equal to the main vortex diameter.

The bifurcation diagram of the main vortex break-up in the Benar cell is shown in Table 2 (the dependence of Ra_m numbers on the bifurcation number m), as well as the harmonic numbers n and vortex diameters $2R_n$ (cm) corresponding to m .

As is seen, the bifurcation numbers Ra_m decreases with the rise of m and cross the level Ra_{cr} ($Ra_{cr} = 657 \div 1708$) at $m = m_{cr} \approx 9-10$. The same m_{cr} value is obtained from the number of the recorded harmonics (in Fig. 4, the maximal n equals to 1849): $m_{cr} \approx E(\log n / \log 2) = E(10.85) = 10$, where $E(x)$ is the integer part of x .

Thus, the origination of the main vortex in the Benar cell and about ten events of its discrete break-up are observed in the pavilion. Vortex diameters, corresponding to the critical values m_{cr} (see Table 2), are within the 0.6–1.2 mm range. They agree with sizes of minimal vortices, existing in air.²

Table 2. Bifurcation diagram in breaking-up main vortex

m	n	Ra_m	$2R_n$, cm
0	1	$1.55 \cdot 10^9$	294
1	2	$5.15 \cdot 10^8$	49.1
2	4	$2.05 \cdot 10^8$	26.8
3	8	$2.76 \cdot 10^6$	4.5
4	16	$4.89 \cdot 10^5$	2.5
5	32	$1.94 \cdot 10^5$	1.5
6	64	$6.86 \cdot 10^4$	0.87
7	128	$2.65 \cdot 10^4$	0.50
8	256	$9.46 \cdot 10^3$	0.26
9	512	1474.1	0.12
10	1024	444.7	0.06
11	2048	67.5	0.05

On the base of the performed analysis, the known stochastic scenarios can be divided into two groups. The first one includes scenarios of origination of periodic flows from laminar ones. Among these scenarios are, first of all, Pomeau–Menneville and Rayleigh–Benar convection. The second group includes break-up scenarios (degeneration) of the appeared vortex periodic flows, the main of them is the Feigenbaum scenario. The Landau–Hopf and Ruelle–Takens (origination of the limiting N -periodic flow) scenarios contain features of both groups.

It follows from the obtained results, that scenarios of both groups are confirmed in the incipient turbulence, a periodic flow is originated (the main vortex in the Benar cell) and breaks up. These processes in principle (in the simplest situations), are confirmed by known solutions of nonlinear equations of hydrodynamics. However, such solutions for a general case are presently unknown.

It is clear, that vortex solutions should exist, since they are experimentally observed. It is also clear, that the stability of vortex solutions will be determined by nonlinear resonances (both between external forces and dissipative processes and between harmonics with commensurable frequencies). Therefore, the mechanism of hydrodynamic turbulence incipience and existence becomes more clear, in which the role of stochastization essentially decreases. Then the turbulence, usually considered as a merely random event, turns to be significantly determinate.

The turbulence determinacy is much stronger than it could be expected from the above analysis. Actually, it follows from the consideration of the threshold-filter damped spectrum harmonics W_T in

Fig. 3, that their greatest maxima (second-order harmonics) can be extracted with the same filter. It turns out that the local structure of second-order harmonics location (between the neighboring first-order ones) is similar to the structure of first-order harmonics location throughout the spectrum W_T . The local self-similarity of the spectrum or, in other words, the fractal structure of the turbulence spectrum is observed.

The frequency dependence of the first- and second-order harmonics (normalized frequencies f_n/f_1 of harmonics) is shown in Fig. 6. This dependence is usually called the “devilish self-similar staircase”; here each inner space between main steps is similar to the whole staircase. Each dash (step) answers its f_n/f_1 value (all these values are integers in Fig. 6). Long dashes correspond to first-order harmonics and short dashes – to second-order ones.

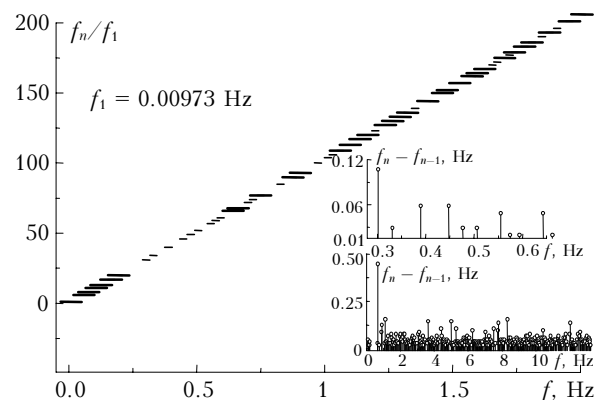


Fig. 6. “Devilish self-similar staircase” (normalized frequencies of the first- and second-order harmonics f_n/f_1). The fragment shows the distance between neighboring harmonics $f_n - f_{n-1}$ ($n = 2, 3, \dots$): between the first-order harmonics for the whole spectrum (the bottom plot) and the second-order harmonics in the 0.19–0.64 Hz range (the upper figure).

The distances between arguments of the neighboring harmonics $f_n - f_{n-1}$ ($n = 2, 3, \dots$) as functions of frequency (of frequencies f_n) are shown in the fragment in Fig. 6: the distances between the first-order harmonics for the whole spectrum W_T (see Fig. 3) are shown in the bottom plot. (As is seen from Fig. 1, it is sufficient to consider only the 0–10 Hz frequency range in the spectrum W_T , without weak noise component, which is caused by the transfer of the motion energy to heat and is observed at frequencies higher than 10 Hz.) The upper plot in the fragment shows the distances between arguments of second-order harmonics for the longest range between the first-order harmonics (0.19–0.64 Hz). As is seen from the “devilish staircase,” other ranges contain a less number of second-order harmonics (because of limited experimental facilities) and are not convenient for the analysis.

The comparison of the top and bottom plots in the fragment confirm a similarity of locations of the

local structures of second-order- and first-order-harmonics in the whole spectrum W_T . The devilish staircase is truly self-similar and the spectrum is fractal. Since second-order maxima are significantly weaker than first-order ones, the second-order harmonics can be called the fractal shadows of the first-order ones. Thus, the process of turbulent flows originating and breaking up is evidently determinate even in weak spectral particulars.

As is known from meteorology, sufficiently stable vortex formations (cells) of different scales exist in the atmosphere. The Ferrel and Hadley cells are the largest among them (up to 5000 km in radius). They can be considered as modifications of Benar cells in a thin spherical layer (at the Earth scale). Somewhat smaller cells (cyclones, anticyclones, thunder-cells, tornados, etc.) exist there as well. The break-up products of these vortices have clearly pronounced deterministic character (corresponding to the non-Kolmogorov incipient turbulence) and are observable in the atmosphere. Open-air measurement data (The Sayan Solar Observatory, July 5, 2007) are shown in Fig. 7 along with the modeled results of the steady-wind transfer through point 5 [Ref. 5, Fig. 2] of a frozen spatial pattern of flows inside the LSVT (sequential slow transfer of data, recorded at seven abreast neighboring points).

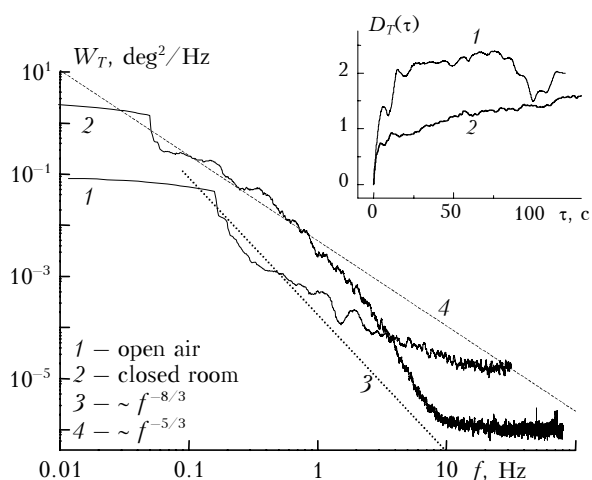


Fig. 7. Kolmogorov turbulence is the result of mixing of determinate vortices. W_T are the smoothed spectra; D_T is the structure functions of temperature fluctuations: curve 1 corresponds to summer daytime measurements in mountains (dry, cloudy). The altitude above the sea level is 2000 m and above the underlying surface it is 32 m. (To avoid superposition, spectral curve 1 is 0.011-Hz shifted left); curve 2 corresponds to wind transfer of a frozen spatial pattern of flows inside the LSVT through one point.

Comparison of Figs. 7, 1, and 9 from Ref. 5 shows that the results for open air, given in Fig. 7, correspond to the determinate incipient non-Kolmogorov turbulence ($W_T \sim f^{-8/3}$ within the inertial interval). On the contrary, transfer of

determinate vortices, formed inside closed rooms, through one point results in the Kolmogorov turbulence ($W_T \sim f^{-5/3}$). Hence, the conclusion can be drawn that the Kolmogorov turbulence is a mixture of determinate different-scale vortices observed in the incipient turbulence.

3. Shifts of spectral lines due to pavilion atmosphere

The above results for the turbulence inside the spectrograph pavilion allow us to answer the practically important question about the influence of air inside specialized telescope rooms on the quality of astronomic observations. First of all, errors of spectral measurements in LSVT are of interest. These errors in the horizontal Ebert scheme are mainly determined by horizontal shifts of spectral lines due to the turbulence and regular refraction in the pavilion atmosphere.

At present, the optical beam shifts in open air are sufficiently well studied,¹³⁻¹⁸ as well as jitter of optical source images^{1,16-19} (usually in telescopes free of interior medium fluctuations). However, in the same Ebert scheme a case appears when several optical elements are separated by air layers with fluctuating characteristics. There appear multiple reflections by a system of mirrors, diffraction grating, etc. in a turbulent medium. Therefore, the problem of optical beam shifts in such multilayer medium becomes more complicated.

This problem can be solved within the Erenfest theorem, generalized to the case of medium with discontinuous characteristics, e.g. a system of adjacent regions separated by planes. The field of the passed wave u_{out} at each plane is connected with the field of incident one u_{in} through some integral transformation. Within each region (layer), the dielectric permittivity ϵ is the sum of the random ϵ_t and regular ϵ_r functions ($\epsilon = \epsilon_t + \epsilon_r$, $\epsilon_1 = \epsilon - 1$). Such discontinuous media are characteristic for segmented atmospheric-optical systems.

In quantum mechanics, the Erenfest theorem expresses the particle coordinates as the product of probability density and potential energy gradient. The theorem was proved again by V.I. Klyatskin and A.I. Kon¹³ for light propagation in a turbulent medium. It expresses the coordinates of beam energy center $\mathbf{R}_c(x)$ at a path of x length via the product of intensity $I(x, \mathbf{R})$ and dielectric permittivity gradient $\nabla_R \epsilon_1(x, \mathbf{R})$. For the medium with discontinuous characteristics this theorem was proved by V.V. Nosov.²⁰

Let an atmospheric-optical system consist of N layers separated by planes at points x_k , $k = 1, 2, \dots, N$ ($x_1 < x_2 < \dots < x_N \leq x$). Preset the boundary condition in x_1 plane. For simplicity, consider the case, when u_{out} is obtained from u_{in} by the ordinary amplitude-phase transformation:

$$\begin{aligned}
 u_{\text{out}}(x_k, \mathbf{R}) &= t_k(\mathbf{R})u_{\text{in}}(x_k, \mathbf{R}), \\
 t_k(\mathbf{R}) &= \exp[-R^2/a_k^2 - ikR^2/(2F_k^2)], \\
 k &= 2\pi/\lambda, \quad t_k(\mathbf{R})t_k^*(\mathbf{R}) = T_k(\mathbf{R}).
 \end{aligned}$$

Here a_k and F_k are the radius and the curvature radius, respectively, of the phase front of an optical element located in x_k plane (k is the wave number). This transformation allows consideration of effects of deflection by systems of lens and apertures, as well as multiple reflections from spherical and flat mirrors.

For coordinates of beam energy center $\mathbf{R}_c(x)$ at a path of x length ($x \geq x_N$) obtain

$$\begin{aligned}
 \mathbf{R}_c(x) &= \sum_{k=1}^{N-1} \left\{ \left(1 - \frac{x - x_N}{F_{\times(k)}} \right) \times \right. \\
 &\times \int_{x_k}^{x_{k+1}} dx' \alpha_k(x') + (x - x_N) [\alpha_k(x_{k+1}) - \alpha_k(x_k)] \left. \right\} + \\
 &+ \left(1 - \frac{x - x_N}{F_{\times(1)}} \right) \beta(x_1) + (x - x_N) \frac{\partial \beta(x)}{\partial x} \Big|_{x=x_1} + \\
 &+ \frac{1}{2p(x_N)} \int_{x_N}^x dx' (x - x') \int d^2R \nabla_R \varepsilon_1(\xi, \mathbf{R}) \gamma(x', \mathbf{R}, 0), \quad (3) \\
 \alpha_k(x') &= -\frac{i}{k} \frac{1}{p(x_N)} \int d^2R T_{\times(k)}(\mathbf{R}) \nabla_{\rho} \gamma(x', \mathbf{R}, \rho) \Big|_{\rho=0}, \\
 \beta(x_1) &= \frac{1}{p(x_N)} \int d^2R \mathbf{R} T_{\times(1)}(\mathbf{R}) \gamma(x_1, \mathbf{R}, 0), \\
 T_{\times(k)}(\mathbf{R}) &= T_{k+1}(\mathbf{R}) T_{k+2}(\mathbf{R}) \dots T_{N-1}(\mathbf{R}) T_N(\mathbf{R}), \\
 F_{\times(k)}^{-1} &= F_{k+1}^{-1} + F_{k+2}^{-1} + \dots + F_{N-1}^{-1} + F_N^{-1}.
 \end{aligned}$$

Here $\alpha_k(x')$ are the angular coordinates in the k th layer of a beam energy center, the intensity of which in the transverse plane is limited by the amplitude of filter function $T_{\times(k)}(\mathbf{R})$ (the filter for symmetrical coaxial optical elements is equivalent to an aperture with radius being the smallest among radiuses of all following elements $k + 1, k + 2, \dots, N$); $\beta(x_1)$ is the similar spatial coordinates of the center in the initial plane x_1 (boundary condition);

$$\begin{aligned}
 \gamma(x', \mathbf{R}, \rho) &= u(x', \mathbf{R} + \rho/2) u^*(x', \mathbf{R} - \rho/2), \\
 \gamma(x', \mathbf{R}, 0) &= I(x', \mathbf{R}),
 \end{aligned}$$

$p(x_N)$ is the flow at the output of the last N th optical element; $\alpha_k(x)$ is can be identified with the angular coordinates of the source image (within the analyzed plane x) after passing through k layers in the case when $t_k(\mathbf{R})$ is a lens and $x \geq x_k$.

The sum in Eq. (3) vanishes at $N = 1$, $T_{\times(k)}(\mathbf{R}) = 1$, $F_{\times(k)}^{-1} = 0$, while $\beta(x_1)$ and $\partial \beta(x)/\partial x|_{x=x_1}$

correspond to usual boundary conditions for beam center coordinates. In this case, the tradition Erenfest theorem follows from Eq. (3), yielding beam center coordinates in open air. At $N = 2$ and $\varepsilon_1 = 0$, there exist spatial coordinates (in the x plane) in the second layer $\mathbf{R}_c(x)$ in Eq. (3) of a source image, located in the initial plane (this is the image jitter provided t_2 corresponds to a lens).

As is seen from Eq. (3), after the wave has passed through N layers, the beam center coordinates are the sum of (random and regular) coordinates of beam shifts in the last layer and coordinates of image displacements by each of N preceding apertures. The displacements of every image, integrated over a previous layer, are also added. Hence, the generalized Erenfest theorem combines beam shifts, image displacements, and regular refraction in compound atmospheric-optical systems.

When proving the theorem, an equation for γ in segmented systems has been obtained, from which a flow equation has been derived. It has been shown that the fluctuating part of a flow is the image jitter of optical dipole (the difference between jitters of two equal contacting apertures). Therefore, the flow dispersion first increases with the rise in β_0^2 ($\beta_0^2 = 1.23 C_n^2 k^7/6 x^{11/6}$) and then decreases. Therefore, the Erenfest theorem allows comparatively simple averaging of the ratio of two random variables in the image displacement vector.

Then, the equation $\nabla_{\rho} \gamma|_{\rho=0} = iI(x, \mathbf{R}) \nabla_{\mathbf{R}} S(x, \mathbf{R})$ in Eq. (3), connecting the wave field u with the phase S and intensity I is used. There are situations, when the phase degrades and is not longer an analytical function, then uncertainties of type $\nabla_{\rho} \gamma|_{\rho=0} = \nabla_{\rho} \delta(\rho)|_{\rho=0} \sim \nabla_{\rho} \delta^2(\rho)$ appear. To eliminate such singularity, it is necessary to change the way of going to limits.

After the phase singularity is eliminated, the ray approximation, used in calculations of the image displacement,¹⁹ yields results coinciding with those from Ref. 18. In particular, equations for dispersion of noncoherent source image displacements, jitter dispersion in strong fluctuations ($\sim \beta_0^{8/5}$), and the dependence on observation plane position are similar. It has been ascertained that the ray approximation in open air virtually coincides with the mean-intensity approximation¹³⁻¹⁸ for beam shifts.

For symmetrical coaxial apertures, $\beta(x_1) = 0$ and $\partial \beta(x)/\partial x|_{x=x_1} = 0$, then $\langle \mathbf{R}_c(x) \rangle = 0$. The mean intensity of a symmetrical beam in a segmented atmospheric optical system can be expressed by the equation

$$\langle I(x, \mathbf{R}) \rangle = \frac{a_c^2(x_1)}{a_c^2(x)} \exp\{-\mathbf{R}^2/a_c^2(x)\} \langle I(x_1, 0) \rangle,$$

where $a_c(x)$ is the effective beam radius at the distance x . Then, in the ray approximation

$$\mathbf{R}_c(x) = \frac{1}{2 \langle p(x_N) \rangle} \int_{x_1}^x d\xi \int d^2\rho \langle I(\xi, \rho) \rangle \nabla_{\perp} \varepsilon_1(\xi, \rho) \times$$

$$\times \{ (x - \xi) \theta(\xi - x_N) + \theta(x_N - \xi) [\eta_1(\xi, \rho) + \eta_2(\xi, \rho)] \},$$

$$\eta_1(\xi, \rho) = \sum_{k=1}^{N-1} \left(1 - \frac{x - x_N}{F_{x(k)}} \right) \times$$

$$\times \int_{\max(\xi, x_k)}^{\max(\xi, x_{k+1})} dx' l(\xi, x') \exp\{-\rho^2 / a_{T,k}^2(\xi, x')\},$$

$$\eta_2(\xi, \rho) = (x - x_N) \sum_{k=1}^{N-1} [l(\xi, x_{k+1}) \exp\{-\rho^2 / a_{T,k}^2(\xi, x_{k+1})\} \times$$

$$\times \theta(x_{k+1} - \xi) - l(\xi, x_k) \exp\{-\rho^2 / a_{T,k}^2(\xi, x_k)\} \theta(x_k - \xi)],$$

$$a_{T,k}^2(\xi, x') = a_{x(k)}^2 l^2(\xi, x'), \quad l^2(\xi, x') = \frac{a_e^2(\xi)}{a_e^2(x')},$$

$$\theta(x) = \begin{cases} 1, & x > 0, \\ 0, & x < 0, \end{cases}$$

$$N \geq 2, \quad a_{x(k)}^{-2} = a_{k+1}^{-2} + a_{k+2}^{-2} + \dots + a_{N-1}^{-2} + a_N^{-2};$$

$$a_{x(k)}^{-2} = 0 \text{ at } N=1.$$

To estimate the errors of optical measurements, an optical path inside the BSVT spectrograph pavilion [Ref. 5, Fig. 1] is presented as a sum of three segments, i.e., entrance window – diagonal mirror (collimator, $F_2=9.5$ m [Ref. 4]); diagonal mirror – grating – camera mirror; and camera mirror – output slit of the spectrograph (CCD-camera⁴). An optical wave is approximately spherical at the first segment, plane at the second one (since the grating does not give wide broadening of the reflected beam,²¹) and a focused beam at the third segment. In this case, all optical elements in the scheme are coaxial and approximately symmetrical and $N=3$ in Eq. (3). To simplify the calculations, take $\nu=1/3$ in Eq. (1) and find path profiles of outer Karman L_0 and inner l_0 turbulence scales from Table 1 at $\nu=1/3$. In calculations, the Karman spectrum model is usually changed to exponential one, therefore, the connection between inner scales, used in these models, should be taken into account.^{16–19} Then the required path profiles C_n^2 are obtained from Table 4 in Ref. 5.

Having calculated the dispersion $\langle \mathbf{R}_c^2 \rangle$, we find that the horizontal random shifts of spectral lines in the optical range ($0.4 \mu\text{m} < \lambda < 0.8 \mu\text{m}$) are about 0.6 arc-second due to pavilion effects ($\beta_0 \approx 0.19$). This result is true for the case when the camera mirror is placed at point 7 [Ref. 5, Fig. 1] and the mutual overlapping of paths in the pavilion is negligible. When the camera mirror is at point 6, the path overlapping should be taken into account. In this case, random shifts can attain 1 arc-second.

Note, that spectral lines shift slowly with a frequency of about 0.01 Hz. This follows from estimations of characteristic frequencies, obtained from data of Ref. 19. Due to low shift frequencies, the incipient turbulence approximates to the regular refraction by its optical properties.

Temperature gradients in the spectrograph pavilion generate not only the Benar cell and the incipient turbulence, but also the regular profile of dielectric permittivity gradient, resulting in regular refraction. To take into account this effect in Eq. (3), preset $\nabla_{\perp} \varepsilon_1 = 2(n-1)(\nabla_{\perp} P/P - \nabla_{\perp} T/T)$, where n is the air refractivity; P is the pressure; T is the average temperature. Then we find that the regular refraction contributes insignificantly in the measurement error, i.e., the side one gives 0.01 and vertical one gives 1 arc-second.

Acknowledgements

This work was financially supported within the SB RAS Complex Integration Project No. 3.2 “Development of adaptive systems of image correction for ground-based telescopes” and the Presidium RAS Program “Day-time astroclimate and problems of adaptive telescope design” (No. 16. P. 3. Project 1).

References

1. V.I. Tatarskii, *Wave Propagation in Turbulent Atmosphere* (Nauka, Moscow, 1967), 548 pp.
2. A.S. Monin and A.M. Yaglom, *Statistical Hydromechanics* (Nauka, Moscow, 1967), V. 1, 696 pp.; (Gidrometeoizdat, St. Petersburg, 1996), V. 2, 742 pp.
3. V.V. Nosov, O.N. Emaleev, V.P. Lukin, and E.V. Nosov, *Atmos. Oceanic Opt.* **18**, No. 10, 756–773 (2005).
4. V.I. Skomorovsky and N.M. Firstova, in: *Solar Physics* (Kluwer Ac. Publ., Belgium, 1996), V. 163, pp. 209–222.
5. V.V. Nosov, V.M. Grigor'ev, P.G. Kovadlo, V.P. Lukin, E.V. Nosov, and A.V. Torgaev, *Atmos. Oceanic Opt.* **20**, No. 11, 926–934 (2007).
6. V.N. Zhigulev and A.M. Tumin, *Turbulence Origination* (Nauka, Novosibirsk, 1987), 283 pp.
7. Y. Pomeau and P. Menneville, *Commun. Math. Phys.* **74**, No. 2, 189–197 (1980).
8. G. Jenkins and D. Watts, *Spectral Analysis and its Applications* (Mir, Moscow, 1971), P. 1, 317 pp; (Mir, Moscow, 1972), P. 2, 285 pp.
9. J.S. Bendat and A.G. Piersol, *Random Data: Analysis and Measurement Procedures* (Wiley, New York, 1971).
10. W.H. Press, S.A. Teukolsky, W.T. Vetterling, and B.P. Flannery, *Numerical Recipes in C*. 2nd ed. (Cambridge Univer. Press, 2002), 994 pp.
11. M.J. Feigenbaum, *J. Statist. Phys.* **19**, No. 1, 25–32 (1978).
12. D. Ruelle and F. Takens, *Comm. Math. Phys.* **20**, No. 2, 167–192 (1971); D. Ruelle, *Math. Intell.* **2**, No. 3, 126–137 (1980).
13. V.I. Klyatskin and A.I. Kon, *Izv. Vyssh. Uchebn. Zaved. SSSR, Ser. Radiofiz.* **15**, No. 9, 1381–1388 (1972).
14. A.I. Kon, V.L. Mironov, and V.V. Nosov, *Izv. Vyssh. Uchebn. Zaved. SSSR, Ser. Radiofiz.* **17**, No. 10, 1501–1511 (1974).

15. V.L. Mironov and V.V. Nosov, *J. Opt. Soc. Am.* **67**, No. 8, 1073–1080 (1977).
16. A.S. Gurvich, A.I. Kon, V.L. Mironov, and S.S. Khmelevtsov, *Laser Radiation in Turbulent Atmosphere* (Nauka, Moscow, 1976), 277 pp.
17. V.L. Mironov, *Laser Beam Propagation in Turbulent Atmosphere* (Nauka, Novosibirsk, 1981), 278 pp.
18. V.E. Zuev, B.A. Banakh, and V.V. Pokasov, *Optics of Turbulent Atmosphere* (Gidrometeoizdat, Leningrad, 1988), 272 pp.
19. V.L. Mironov, V.V. Nosov, and B.N. Chen, *Izv. Vyssh. Uchebn. Zaved. SSSR, Ser. Radiofiz.* **23**, No. 4, 461–469 (1980); *Proc. of the 2nd Workshop in Atmospheric Optics* (Tomsk, 1980), P. 2, pp. 101–103.
20. V.V. Nosov, in: *XIV Int. Symp. "Atmospheric and ocean optics. Atmospheric Physics,"* Tomsk (2007), pp. 101–103.
21. V.P. Shestopalov et al., *Resonance Wave Scattering. Diffraction Gratings* (Nauk. dumka, Kiev, 1986), V. 1, 232 pp.